MANIPULATION

Robotic manipulation of cardiomyocytes to identify gap junction modifiers for arrhythmogenic cardiomyopathy

Wenkun Dou[1,2,3]†, Guanqiao Shan[1,2]†, Qili Zhao[4,5]†, Manpreet Malhi[3,6]†, Aojun Jiang[2], Zhuoran Zhang[7], Andrés González-Guerra[8], Shaojie Fu[4], Junhui Law[2], Robert M. Hamilton[9,10], Juan A. Bernal[8], Xinyu Liu[2,11]*, Yu Sun[2,11,12,13]*, Jason T. Maynes[3,6,14]*

Arrhythmogenic cardiomyopathy (ACM) is a leading cause of sudden cardiac death among young adults. Aberrant gap junction remodeling has been linked to disease-causative mutations in plakophilin-2 (*PKP2*). Although gap junctions are a key therapeutic target, measurement of gap junction function in preclinical disease models is technically challenging. To quantify gap junction function with high precision and high consistency, we developed a robotic cell manipulation system with visual feedback from digital holographic microscopy for three-dimensional and label-free imaging of human induced pluripotent stem cell–derived cardiomyocytes (iPSC-CMs). The robotic system can accurately determine the dynamic height changes in the cells' contraction and resting phases, microinject drug-treated healthy and diseased iPSC-CMs in their resting phase with constant injection depth across all cells, and deposit a membrane-impermeable dye that solely diffuses between cells through gap junctions for measuring the gap junction diffusion function. The robotic system was applied toward a targeted drug screen to identify gap junction modulators and potential therapeutics for ACM. Five compounds were found to dose-dependently enhance gap junction permeability in cardiomyocytes with *PKP2* knockdown. In addition, PCO 400 (pinacidil) reduced beating irregularity in a mouse model of ACM expressing mutant PKP2 (R735X). These results highlight the utility of the robotic cell manipulation system to efficiently assess gap junction function in a relevant preclinical disease model, thus providing a technique to advance drug discovery for ACM and other gap junction–mediated diseases.

INTRODUCTION

Arrhythmogenic cardiomyopathy (ACM), also referred to as arrhythmogenic right ventricular cardiomyopathy/dysplasia, is a primarily inherited disease of the heart characterized by cell-to-cell conduction defects, progressive fibrofatty replacement of the myocardium, and high risk of fatal ventricular arrhythmias (*1*). The disease is a leading cause of sudden cardiac death among young people, accounting for 14% of associated mortalities in the age group of 1 to 35 years (*2*). The development of therapeutics to mitigate early arrhythmic risk is critical for the prevention of sudden cardiac arrest; however, there is currently a lack of preclinical tools to model disease pathology in human cells with sufficient throughput to screen a large number of compounds.

ACM is most commonly associated with mutations in genes encoding desmosomal proteins. Desmosomes are intercellular junctions that are necessary to maintain cell-cell adhesion, particularly in tissues that are subject to mechanical stress, such as the skin and heart. Depending on the geographic region, up to 78% of mutations linked to familial ACM are found in the gene encoding the desmosomal protein plakophilin-2 (PKP2) (*3*, *4*). In cardiac desmosomes, PKP2 links adjacent sarcolemmal membranes by facilitating the interactions among desmoplakin, plakoglobin, and desmosomal cadherins (*5*). In addition to its role in maintaining desmosome stability and the mechanical integrity of the myocardium, PKP2 is a component of the connexome, where it interacts with the gap junctional pore protein connexin-43 (Cx43) (*6*). Gap junctions facilitate the rapid flow of ions and small molecules between cells and are critical for action potential propagation in cardiomyocytes (*7*). Genetic deletion or mutation of PKP2 alters both the expression and subcellular localization of Cx43, resulting in aberrant gap junction remodeling (*8*).

To study gap junction permeability, scrape loading of dyes is a simplistic method whereby a scratch by a razor blade is made in a confluent monolayer of cells to expose gap junctions and allow for dye incorporation from culture media (*9*). This technique causes injury to cells and does not accurately reflect gap junction function (*10*). More advanced techniques established in recent years introduce fluorescent probes by single-cell microinjection (*11*). Microinjection was traditionally performed manually with limited throughput and reproducibility. To overcome the limitations of manual microinjection, robotic adherent cell manipulation systems were developed for microinjecting static cells (instead of beating cells) (*12*, *13*). In these systems, to determine the depth information along the *z* axis using two-dimensional (2D) microscopy visual feedback, contact detection

[1]Institute of Robotics and Intelligent Systems, Dalian University of Technology, Dalian, Liaoning, China. [2]Department of Mechanical and Industrial Engineering, University of Toronto, Toronto, ON, Canada. [3]Program in Molecular Medicine, Hospital for Sick Children, Toronto, ON, Canada. [4]Institute of Robotics and Automatic Information System and the Tianjin Key Laboratory of Intelligent Robotics, College of Artificial Intelligence, Nankai University, Tianjin, China. [5]Institute of Intelligence Technology and Robotic Systems, Shenzhen Research Institute of Nankai University, Shenzhen, China. [6]Department of Biochemistry, University of Toronto, Toronto, ON, Canada. [7]School of Science and Engineering, Chinese University of Hong Kong (Shenzhen), Shenzhen, China. [8]Centro Nacional de Investigaciones Cardiovasculares (CNIC), Madrid, Spain. [9]Department of Paediatrics, Division of Cardiology, Hospital for Sick Children, Toronto, ON, Canada. [10]Program in Translational Medicine, Hospital for Sick Children, Toronto, ON, Canada. [11]Institute of Biomaterials and Biomedical Engineering, University of Toronto, Toronto, ON, Canada. [12]Department of Electrical and Computer Engineering, University of Toronto, Toronto, ON, Canada. [13]Department of Computer Science, University of Toronto, Toronto, ON, Canada. [14]Department of Anesthesia and Pain Medicine, Hospital for Sick Children, Toronto, ON, Canada.
*Corresponding author. Email: yu.sun@utoronto.ca (Y.S.); jason.maynes@sickkids.ca (J.T.M.); xinyu.liu@utoronto.ca (X.L.)
†These authors contributed equally to this work.

algorithms were developed to detect either the substrate position or the top surface of the cell (*14*, *15*). Because cells vary in height, contacting and deforming each cell with an end effector, such as a glass micropipette, to determine cell height is time-consuming.

Unlike the manipulation of static cells, robotic manipulation of beating cardiomyocytes has not been attempted because of their dynamic height changes and distinct contraction and resting phases. Similar to performing surgery on a beating heart (*16*), which necessitates the synchronization of the surgical tool's motion and the heart's motion, for the microinjection of beating cardiomyocytes, the dynamic height changes of the cell must be accurately measured to determine its periodic contraction and resting phases, and the microinjection should be completed within the resting duration, which is approximately 0.3 s.

Here, we report a robotic cell manipulation system that incorporates digital holographic microscopy (DHM) imaging for 3D visual feedback to perform high-precision microinjection of beating cardiomyocytes. The system is capable of accurate measurement of each cardiomyocyte's height in real time, in situ segmentation of cell nucleus regions, and microinjection of spontaneously beating induced pluripotent stem cell–derived cardiomyocytes (iPSC-CMs) during the temporal resting phase with a constant injection depth across all cells. We have adopted the robotic system to study gap junction permeability in healthy and diseased iPSC-CMs. We performed a targeted drug screen with the goal of identifying potential antiarrhythmic therapies for ACM, which were subsequently validated in an animal model of the disease. The obtained results demonstrated that our robotic system allows for rapid and reliable assessment of gap junction permeability in vitro, facilitating therapeutic development for diseases characterized by aberrant gap junction activity, such as ACM.

RESULTS

Robotic microinjection of beating cardiomyocytes

As shown in Fig. 1A and fig. S1, the robotic system consists of an inverted optical microscope, a DHM unit, a robotic micromanipulator, and custom-designed control software for automated microinjection of dynamically beating iPSC-CMs. Because traditional microinjection pipettes are not able to reach the bottom of standard 96-well microplates from a tilting angle, we fabricated custom Z-shaped microinjection pipettes (Fig. 1B; also see Materials and Methods for details). iPSC-CMs were seeded in the wells of the microplate and incubated with each drug for 24 hours before the measurement of the gap junction diffusion function by our robotic system. An overview of the system's control architecture is shown in fig. S2. To microinject each cell, the micropipette tip was first moved horizontally (in the *x*-*y* plane) and positioned 3 μm from the nucleus region of the target cell along the *x* axis. The visual feedback of cell height from DHM images was used by the system to control the micropipette to approach the target cell vertically along the *z* axis. When the target cell entered its resting phase, the micropipette tip was controlled to reach the contact point on the cell membrane and then to the dye deposition point with an injection depth of 2 μm (fig. S3).

Movie S1 shows the dynamic beating motions of an iPSC-CM monolayer under both bright-field and DHM imaging. Because cardiomyocytes are thin and transparent, measuring their dynamic motions and height changes under conventional intensity-based light microscopy is challenging (Fig. 1C, i). Instead, DHM imaging was used to effectively detect the phase shifts of transmitted light when passing through the transparent specimens (*17*), hence providing quantitative visualization of cell morphologies (Fig. 1C, ii) and their beating dynamics noninvasively (resolution along the *z* axis: ~106 nm; see Materials and Methods for details). Live staining images of the same iPSC-CM monolayer were also captured, and the absolute height of each cell was measured on a laser scanning confocal microscope (Fig. 1D and movie S2). The absolute cell height data (Fig. 1D, ii) were used as a benchmark to determine the mean intracellular refractive index $\overline{n}_c = 1.380 \pm 0.005$, which was further used for label-free height calculation of dynamic beating cardiomyocytes (see Materials and Methods for details). Figure 1E shows the cross-sectional height profiles obtained from the DHM phase image matched with those measured from the fluorescent live-staining image at the same monolayer location. The results showed that the average cell height of the iPSC-CMs ranged from 3.21 to 6.85 μm. In addition, we measured the average heights of the nucleus region and the cytoplasm region of each cell in their resting phase and contraction phase ($n = 20$ cells). The average height of the nucleus region was found to be 4.93 ± 0.62 μm in the resting phase and 5.41 ± 0.75 μm in the contraction phase, and the average height of the cytoplasm region was measured to be 3.68 ± 0.55 μm in the resting phase and 3.41 ± 0.45 μm in the contraction phase (Fig. 1F). For each cell, the average height of the nucleus region was ~1.5 times higher than that of the cytoplasm region in both the resting phase and contraction phase.

High-precision microinjection of dynamic beating cardiomyocytes was facilitated by the visual feedback information from DHM imaging, including the locations of nucleus regions, cell height variations, and the cardiomyocyte beating dynamics. Nucleus segmentation was conducted on the basis of the grayscale intensity differences on the live DHM phase images and was fitted into elliptical shapes (Fig. 1G). To evaluate the segmentation accuracy, cell nuclei were live-stained with Hoechst 33342. Results showed that our algorithm accurately segmented the nucleus regions of iPSC-CMs with either a single nucleus or double nuclei (fig. S4). The cell penetration site was set at a lateral distance of 3 μm from the segmented nucleus boundary to ensure dye diffusion in the cytoplasm and prevent damage to the cell nuclei (*18*). In addition, the dynamic vertical displacements of iPSC-CMs were also detected on the basis of DHM imaging, as shown in Fig. 1H. A height change as large as 0.51 ± 0.13 μm ($n = 5$ independent monolayers) occurred in the *z* axis as the cells contracted. To ensure reproducibility and cell viability, microinjection was only conducted in the cell's resting phase with a preset injection depth (see movie S3).

Cardiomyocytes are mechanosensitive cells that alter their behavior in response to mechanical stimuli (*19*). The micropipettes used in the experiments had conical tips (Fig. 1B) and thereby could elicit a greater mechanical stimulus with an increasing injection depth. We intentionally varied the injection depth to measure the effect of mechanical stimulation on fluorescent dye transfer through cardiac gap junctions, the success rate of dye deposition, and cell viability. The errors of injected depth were measured to be 0.11 ± 0.02 μm, 0.14 ± 0.02 μm, and 0.15 ± 0.03 μm ($n = 20$ cells for each injection depth) when the injection depths were set at 1, 2, and 3 μm, respectively (fig. S5). Cardiomyocytes were microinjected with propidium iodide, a fluorescent membrane–impermeable dye that stains nucleic acids (Fig. 2A). Propidium iodide has previously been validated to measure dye transfer through gap junctions by cell

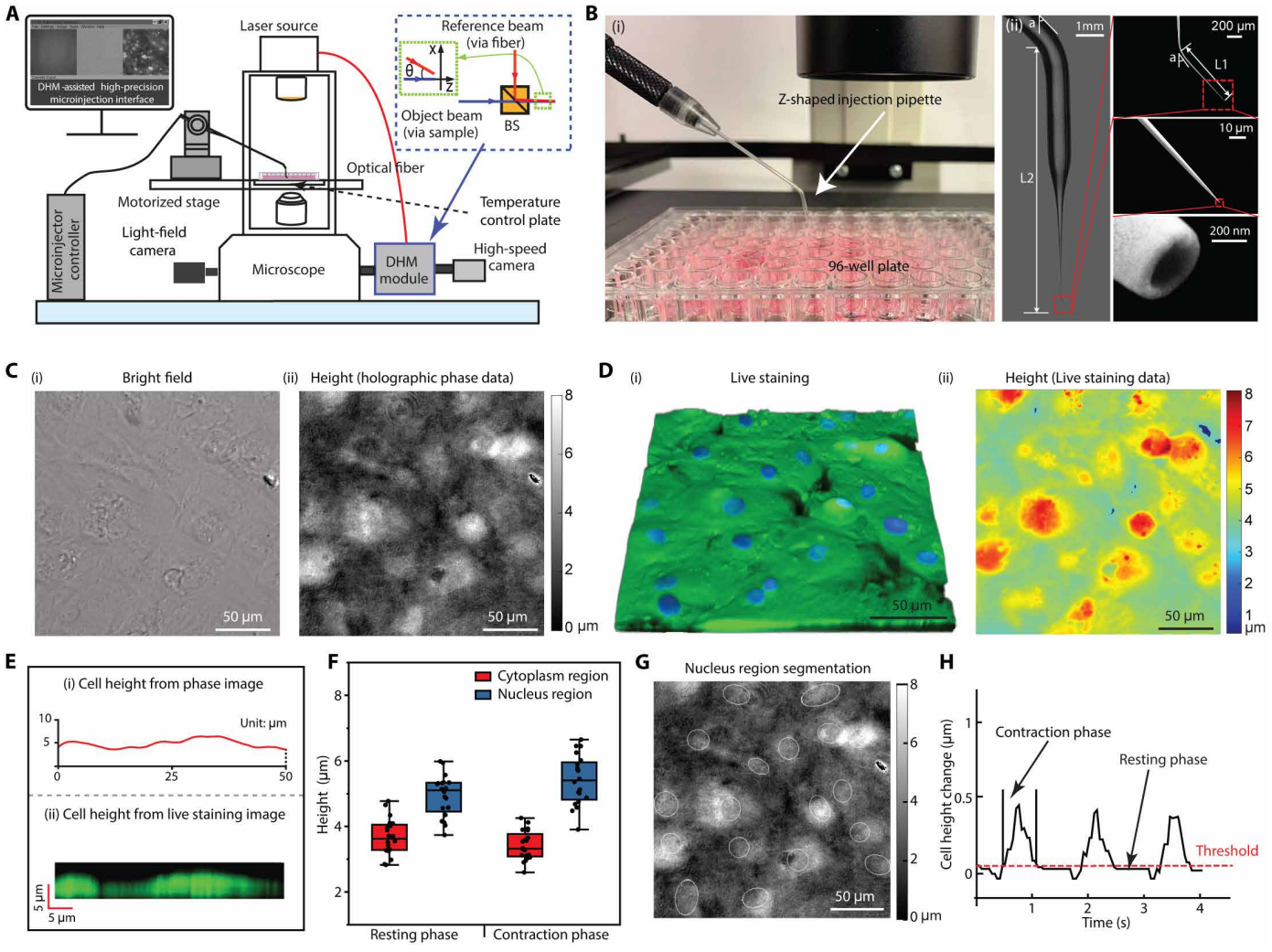

Fig. 1. DHM-assisted robotic system for high-precision microinjection of beating cardiomyocytes. (**A**) Robotic system setup, consisting of an inverted microscope, a DHM unit, a microinjector controller, a robotic micromanipulator, and custom-designed control software. (**B**) The Z-shaped micropipette allows for microinjection of adherent cells at a 45° angle in multiwell formats ($L1 = 1$ mm, $L2 = 1$ cm). (**C**) Bright-field and holographic phase images of an iPSC-CM monolayer under the same imaging field. (**D**) Live staining of iPSC-CM monolayer by calcein (green) and Hoechst (blue) to quantify cell height as the benchmark for calculating the mean intracellular refractive indexes of iPSC-CMs. (**E**) Cross-sectional cell height of the same cardiomyocytes obtained by DHM phase imaging and live staining fluorescence imaging. (**F**) Heights of the nucleus region and the cytoplasm region in the resting phase and in the contraction phase when the cell beating amplitude reached its maximum ($n = 20$ cells). The box plot indicates the complete range (whiskers), interquartile range (box), and median (line) of the measurement. (**G**) Nucleus segmentation based on the grayscale intensity differences between the nucleus regions and the cytoplasm regions in DHM phase images. (**H**) Representative vertical cell displacement curve. Microinjection was only performed during the resting phase.

microinjection (*20*). Upon injection, the dye can only diffuse between cells through gap junctions. Dye transfer was calculated on the basis of the number of neighboring cells whose nuclei were fluorescently positive (see fig. S6 and movie S4 for continuous monitoring of dye transfer). By varying the injection depth to 1, 2, and 3 μm, an average dye transfer to 3.2 ± 0.1, 2.8 ± 0.1, and 2.4 ± 0.1 cells, respectively, was observed 2 min after injection ($n = 50$ microinjected cells per injection depth; Fig. 2B). Although greater injection depth appeared to negatively influence gap junction permeability, this effect was only transient, and cardiomyocytes recovered gap junction permeability to baseline levels within 6 min of microinjection ($P > 0.05$) (Fig. 2B). As summarized in table S1, when the injection depth was set at 2 μm, the robotic system achieved a 95.2 ± 0.9% success rate of dye deposition and a 90.1 ± 1.1% cell survival rate. The approximately 5% failure rate was attributed to the low number of cells that the micropipette was not able to penetrate. When the injection depth was increased to 3 μm, the system achieved a success rate of 99.3 ± 0.4% given that almost all of the cells were penetrated; however, the cell survival rate decreased to 78.3 ± 1.7%.

To investigate cell membrane deformation, the robotic microinjection process was imaged under a spinning disk confocal microscope (Nikon, CSU-W1). Cell membranes were live stained by CellMask Green, and the micropipette tip was fluorescently labeled by Alexa Fluor 647-BSA. On the basis of the cross-sectional views captured by confocal imaging (fig. S7), time-dependent membrane

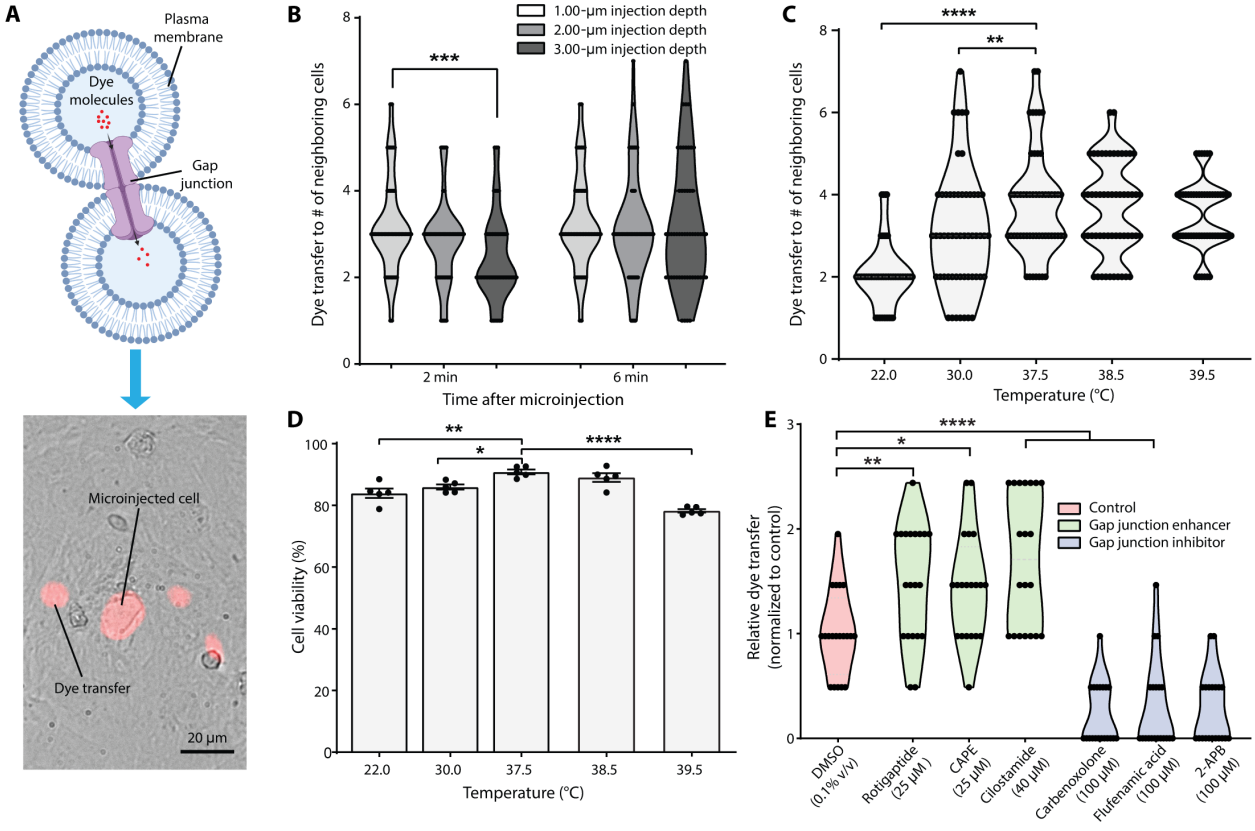

Fig. 2. Microinjection of cardiomyocytes with propidium iodide to measure gap junction function. (**A**) A representative fluorescent image of an iPSC-CM microinjected with propidium iodide, a membrane-impermeable nucleic acid stain. Dye diffusion to adjacent cells occurs solely through gap junctions and was quantified from the number of cells neighboring the microinjected cell with nuclei that were positive for a fluorescent signal. (**B**) Dye diffusion through gap junctions was negatively correlated with injection depth 2 min after injection; however, cells recovered full gap junction function by 6 min after injection ($n = 50$ microinjected cells per injection depth and time point). Distributions in dye transfer among microinjected cells are represented with a violin plot. (**C**) Quantification of dye transfer in microinjected iPSC-CMs under different temperatures. Dye diffusion through gap junctions increased as the temperature increased from 22.0 to 37.5°C and then decreased as the temperature further increased to 39.5°C ($n = 50$ microinjected cells per temperature). (**D**) Cell viability also increased from 22.0 to 37.5°C and then decreased at higher temperatures ($n = 5$ independent monolayers). (**E**) Dye diffusion was measured in iPSC-CMs treated with known enhancers of gap junction activity (25 μM rotigaptide, 25 μM CAPE, and 40 μM cilostamide) and gap junction inhibitors (100 μM carbenoxolone, 100 μM flufenamic acid, and 100 μM 2-APB) ($n = 20$ microinjected cells per drug). Data were calculated relative to cells treated with DMSO (0.1% v/v). Values are reported as means ± SEM. Statistics were calculated via a one-way ANOVA with a Dunnett's multiple comparisons post hoc test (*$P < 0.05$, **$P < 0.01$, ***$P < 0.001$, and ****$P < 0.0001$).

deformation was quantified. Cell membrane deformation reached a maximum (1.68 ± 0.06 μm, $n = 20$ cells) when the micropipette tip arrived at the dye deposition point, and the penetration depth was determined to be 0.38 ± 0.04 μm ($n = 20$ cells). In addition, we compared the cell volume before and after microinjection and found no difference within the confocal microscope's imaging resolution, which can be attributed to the vast volume of a cardiomyocyte (6207 ± 1106 fl, $n = 20$ cells) when compared with the deposited volume of 25 fl by microinjection.

Conductance through gap junctions has previously been shown to be sensitive to temperature (*21*). Thus, during the optimization of our microinjection parameters, we quantified dye transfer in iPSC-CMs under different temperatures using a heating plate with a temperature control error of 0.1°C. Dye transfer through gap junctions was found to increase as the temperature increased from 22.0 to 37.5°C and then decreased as the temperature further increased to 39.5°C (Fig. 2C). In addition, cell viability was measured using Live/Dead Cell Imaging Kits (R37601, Thermo Fisher Scientific) and was also found to increase from 22.0 to 37.5°C and then decrease at higher temperatures (Fig. 2D), which can be attributed to overheating-induced myocardial dysfunctions, such as sodium channel blocking (*22*) and alteration of metabolic activities (*23*). On the basis of these collective findings, we determined the optimal conditions for microinjection of iPSC-CMs to be 2-μm injection depth, 37.5°C ambient temperature, and collection of measurements 6 min after injection to ensure sufficient time for recovery of gap junction permeability.

Validation of the robotic microinjection assay using known gap junction modulators

We selected six drugs known to modulate gap junction activity to validate the performance of our robotic iPSC-CM microinjection system, including three gap junction enhancers [rotigaptide, caffeic acid phenethyl ester (CAPE), and cilostamide] and three gap junction inhibitors [carbenoxolone, flufenamic acid, and 2-aminoethoxydiphenyl borate (2-APB)] (Fig. 2E and fig. S8). The measurement of dye transfer by our robotic microinjection assay was performed after

incubating the iPSC-CMs with each drug for 24 hours. The gap junction enhancers were all found to increase gap junction permeability relative to 0.1% v/v dimethyl sulfoxide (DMSO)–treated cells. Rotigaptide (25.0 μM), CAPE (25.0 μM), and cilostamide (40.0 μM) increased dye transfer by 48.8 ± 12.5%, 43.9 ± 11.5%, and 70.7 ± 14.4%, respectively ($P < 0.01$ for all drugs). Conversely, the gap junction inhibitors carbenoxolone (100.0 μM), flufenamic acid (100.0 μM), and 2-APB (100.0 μM) decreased dye transfer by 78.1 ± 6.6%, 70.7 ± 9.6%, and 73.2 ± 7.5%, respectively ($P < 0.01$ for all drugs) (Fig. 2E). These results demonstrated that our automated system was capable of appropriately determining changes to gap junction permeability in iPSC-CMs. Compared with Lucifer yellow, which produced a fluorescent signal diffuse throughout the cell area, propidium iodide produced a strong fluorescent signal localized to the nuclei for easier quantification (fig. S8).

Knockdown of *PKP2* in iPSC-CM monolayers produces an ACM phenotype

To model the loss of PKP2 function commonly observed in ACM, we performed lentiviral short hairpin RNA (shRNA) knockdown of *PKP2* in iPSC-CM monolayers. A 69.6 ± 6.0% decrease in PKP2 protein levels was observed by Western blot 14 days after transduction, quantified by densitometry ($P < 0.001$) (Fig. 3A). Protein knockdown caused a time-dependent change in the contractility of cardiomyocytes (Fig. 3B and fig. S9). Relative to nonsilenced controls, *PKP2* knockdown decreased beat amplitude (contractility) by 16.1 ± 2.6%, 22.2 ± 2.2%, and 29.0 ± 2.4% at 7, 14, and 21 days after transduction, respectively ($P < 0.0001$ at all time points) (Fig. 3B). Compared with control iPSC-CMs, PKP2-deficient cells exhibited a 26.3 ± 1.6% reduction in dye transfer ($P < 0.0001$) (Fig. 3C). The expression and localization of Cx43 were probed by immunofluorescence microscopy. The knockdown of *PKP2* was found to decrease the surface expression of Cx43 and increase the intracellular localization of the protein, indicative of perturbed gap junction formation (Fig. 3D). In addition, we have recently reported that *PKP2* knockdown in iPSC-CMs causes notable cell-to-cell conduction defects, characterized by decreased conduction velocity and increased spatial variance of beating trajectories across cell monolayers (*24*). Together, the observed effects of *PKP2* knockdown on iPSC-CM contractility and gap junction permeability are representative of pathologic changes associated with ACM (*25*).

Identification of gap junction enhancers using robotic microinjection on iPSC-CMs with knockdown of *PKP2*

The development of therapeutics targeting gap junction dysfunction remains a relatively unexplored area of research, despite its known implications on arrhythmogenesis (*26*). We performed a targeted screen for modulators of gap junction permeability using our robotic microinjection system on iPSC-CM functional monolayers after *PKP2* knockdown. Two weeks after transduction, knockdown cells were tested against the SCREEN-WELL ion channel ligand library (Enzo Life Sciences) consisting of 70 known ion channel modulators. Six additional modifiers of cardiac activity or gap junction function were also studied. From the screen, five compounds were found to enhance gap junction permeability by greater than 50% relative to 0.1% v/v DMSO-treated cells ($P < 0.05$), as measured by dye transfer (Fig. 4). Ranked in descending order from highest efficacy, these compounds include PQ15 (investigational cancer therapeutic) (*27*), tolazamide (K^+ channel blocker) (*28*), flecainide (Na^+ channel blocker) (*29*), PCO 400 (K^+ channel opener) (*30*), and quinine (K^+ channel blocker) (*30*). Each compound demonstrated dose-dependent enhancement of gap junction permeability when tested over a range of concentrations (fig. S10). In addition to having identified potential therapeutic modulators of gap junctions, these results highlight the utility of the robotic microinjection screen for efficient quantification of gap junction permeability in a clinically relevant disease model.

PCO 400 reduces beating irregularity in mice expressing mutant PKP2 (R735X)

We investigated the cardiac activity of our screening hits using an established mouse model of ACM. The PKP2-R735X mutation has been shown to induce an ACM phenotype in mice and gives rise to truncated PKP2 products found in patients with ACM (*25*). In our experiment, mice were transduced with AAV-PKP2 (wild-type) or AAV-R735X (mutant) and treated 6 weeks after transduction with a single dose of each drug by intraperitoneal injection. Automated electrocardiography (ECG) analysis (see Materials and Methods) was used to quantify changes to mean heart rate (in beats per minute), beating irregularity [root mean square of successive differences (RMSSD) of successive beats], and QRS duration (in milliseconds, representing the time interval for the electrical depolarization of the ventricles). Flecainide and PCO 400 were found to cause functional changes in the hearts of mice (Fig. 5 and fig. S11). In wild-type and mutant mice, respectively, flecainide (20 mg/kg) reduced mean heart rate (in beats per minute) by 10.5 ± 4.3% ($P < 0.05$) and 22.6 ± 5.3% ($P < 0.001$) and increased QRS duration (in milliseconds) by 66.7 ± 9.0% ($P < 0.01$) and 80.2 ± 8.7% ($P < 0.01$) (Fig. 5, A, and E). Flecainide did not reduce beating irregularity under nonstressed conditions in either group of mice (Fig. 5C). PCO 400 (1 mg/kg) did not significantly alter mean heart rate or QRS duration ($P > 0.05$) (Fig. 5, B and F); however, the drug reduced beating irregularity in mutant mice (59.8 ± 5.8% reduction in RMSSD of successive beats 5 min after drug treatment, $P < 0.05$) (Fig. 5D).

DISCUSSION

Across most mammalian tissue types, gap junctions play a pivotal role in mediating cell-cell communication (*31*). The importance of these intercellular structures is highlighted by their involvement in a broad spectrum of human diseases, including skin (*32*), joint (*33*), inflammatory (*34*), neurodegenerative (*35*), and heart diseases (*26*). Hence, gap junctions are a key therapeutic target, but measurement of gap junction function in preclinical disease models is technically challenging. Our robotic approach was able to measure cell height and conduct microinjection with a consistent injection depth across all cardiomyocytes in their resting phase without the need to perform contact detection on each cell. The system achieved the microinjection of beating cardiomyocytes at a speed of ~20 cells/min with a success rate of dye deposition of 95.2% as well as high reproducibility and postinjection cell viability.

In robotic micromanipulation, standard optical microscopy provides high-resolution visual feedback in two dimensions (*x*-*y* plane) (*36*), but accurately determining the *z* positions of the end effector and the object to manipulate has been a challenge (*37*). A few methods have been proposed to address this challenge, but all have limitations. The focus-defocus approach estimates *z*-coordinate differences with a limited resolution of approximately 5.8 μm under

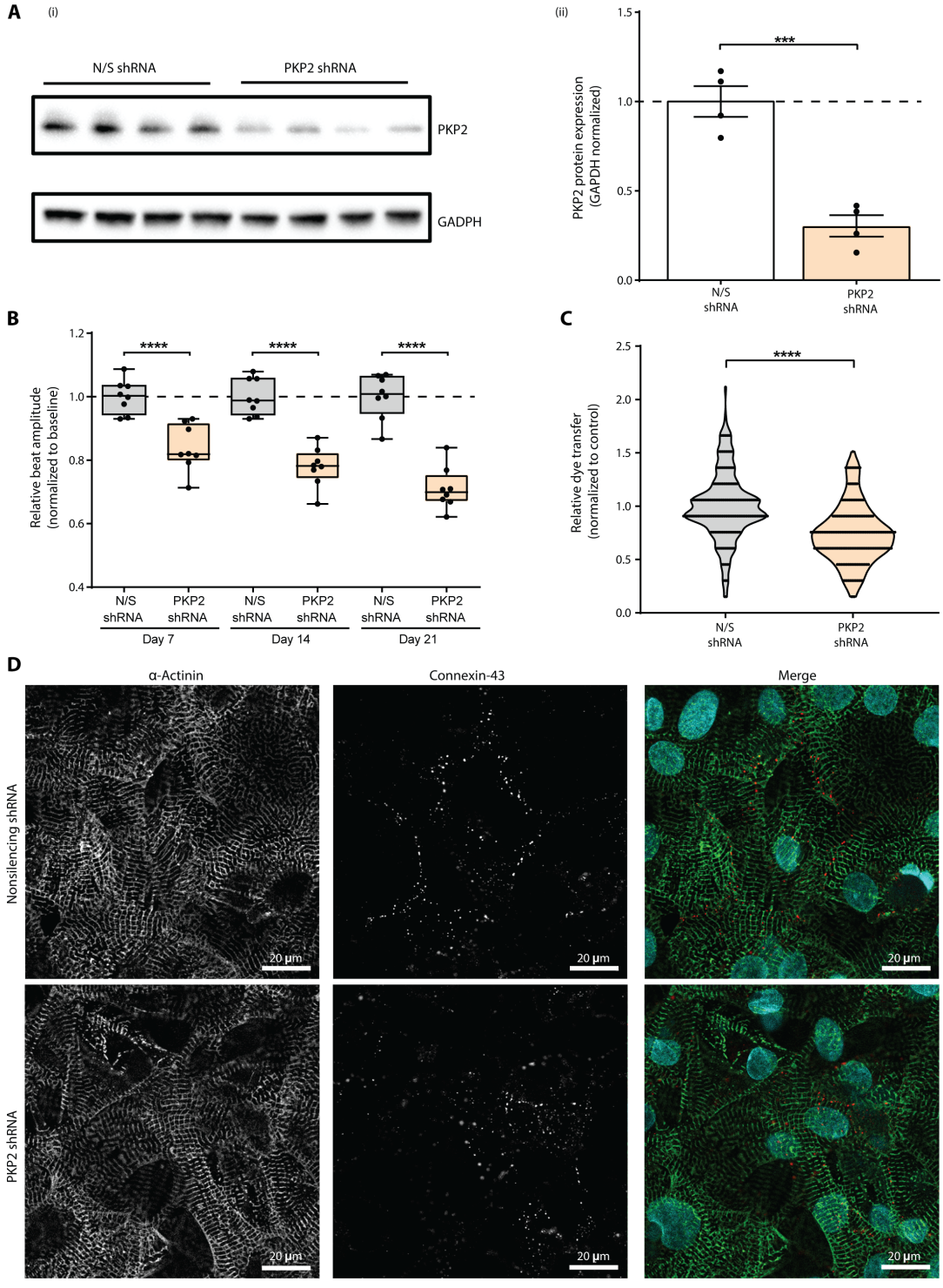

Fig. 3. Functional characterization of iPSC-CMs with *PKP2* knockdown. (**A**) Knockdown of *PKP2* was performed in iPSC-CMs by lentiviral delivery of a pGIPZ shRNA plasmid. Reduction in glyceraldehyde-3-phosphate dehydrogenase (GAPDH)–normalized PKP2 protein levels was observed by Western blot 14 days after transduction relative to the nonsilencing (N/S) control ($n = 4$ cell lysates). Protein levels were quantified by densitometry. (**B**) Analysis of iPSC-CM beat amplitude (contractility). *PKP2* knockdown was found to decrease beat amplitude compared with iPSC-CMs transduced with an N/S control ($n = 8$ independent monolayers). The box plot indicates the complete range (whiskers), interquartile range (box), and median (line) of the measurement. (**C**) Measurement of gap junction permeability in iPSC-CMs 14 days after transduction. Compared with N/S control cells, *PKP2* knockdown caused a reduction in dye transfer to neighboring cardiomyocytes ($n = 200$ microinjected cells). Distributions in dye transfer among microinjected cells are represented with a violin plot. (**D**) Representative immunofluorescent images of Cx43 expression and localization in iPSC-CMs 14 days after transduction. Knockdown of *PKP2* caused a decrease in Cx43 localization at the boundaries between cells where gap junctions are formed. Values are reported as means ± SEM normalized to N/S control. Statistics were calculated via a two-sided Student's *t* test or a one-way ANOVA with a Bonferroni's multiple comparisons post hoc test (***$P < 0.001$ and ****$P < 0.0001$).

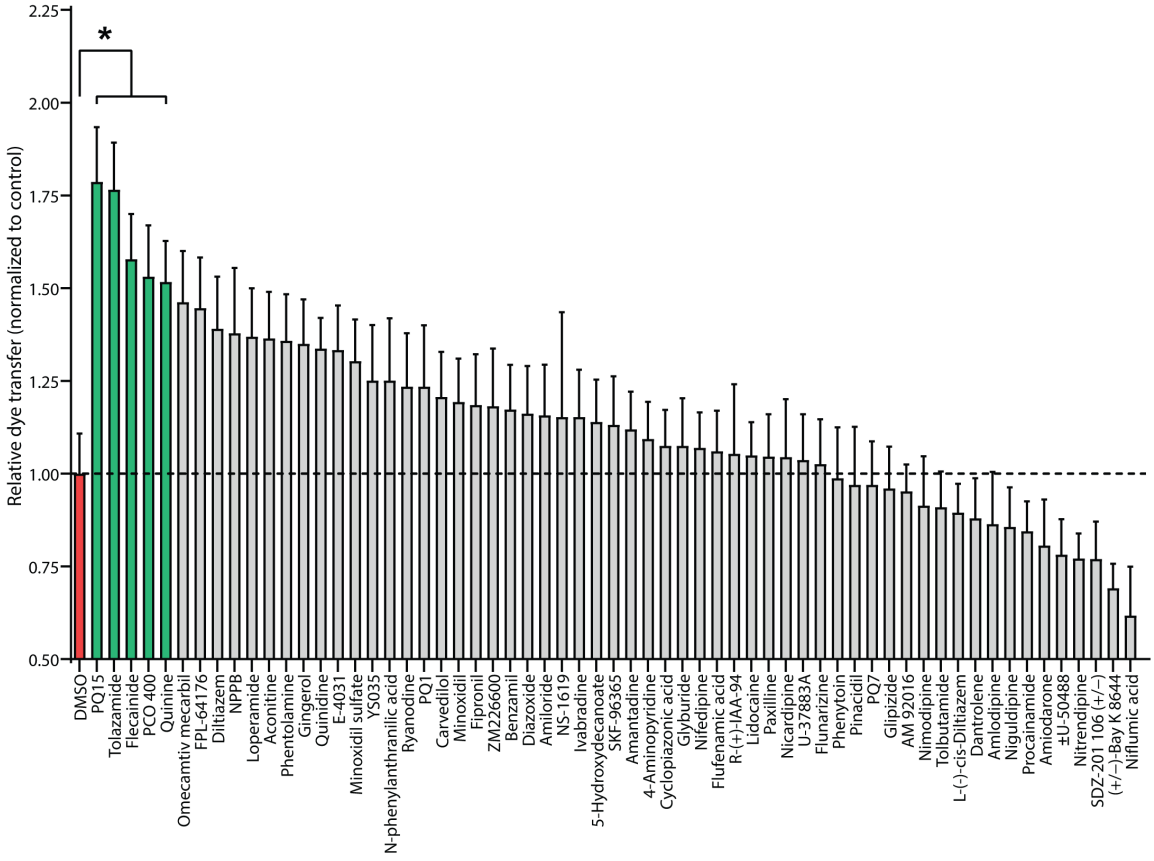

Fig. 4. Robotic screening of iPSC-CMs with *PKP2* knockdown to identify enhancers of gap junction function. Two weeks after lentiviral transduction, iPSC-CMs with *PKP2* knockdown were screened against 76 compounds ($n = 20$ microinjected cells per drug). Five compounds (PQ15, tolazamide, flecainide, PCO 400, and quinine) were found to enhance gap junction function by greater than 50% relative to knockdown cells treated with a 0.1% v/v DMSO control. Compounds that caused overt cytotoxicity in iPSC-CMs were excluded from the analysis. Values are reported as means ± SEM normalized to DMSO control. Statistics were calculated via a one-way ANOVA with a Dunnett's multiple comparisons post hoc test (*$P < 0.05$).

×20 magnification (*37*). Confocal microscopy enables accurate 3D imaging, but the specimen must be fluorescently labeled (*38*). To obtain a submicrometer resolution without fluorescent labeling, vision-based contact detection methods were developed to determine the z coordinate of the locally contacted points, but they are complex and time-consuming (*15*). On the contrary, our robotic system incorporated label-free DHM imaging and used quantitative phase information to obtain visual feedback three-dimensionally and accurately determine the height of each beating cardiomyocyte in both their resting phase and contraction phase as well as the 3D position of the cell nucleus. With such 3D information, the robotic system performed microinjection with a consistent injection depth and avoidance of mechanical damage to the cell nucleus.

Unlike static cells, the beating behavior of cardiomyocytes causes dynamic changes in cell heights. On the basis of 3D visual feedback, the robotic system accurately determined the spatial and temporal transient cardiomyocyte height changes caused by cell contraction. Once the cell entered the resting phase, the robotic system controlled the micropipette to move to the contact point on the cell membrane, deform and penetrate the cell membrane, deposit dye in the cell, and retract out of the cell, with all the steps completed in less than 0.3 s, within the cell's resting phase. A detailed investigation of cell membrane deformation and recovery confirmed that maximum membrane deformation before micropipette penetration for most cells was well within 1.6 μm, and the micropipette deposited the dye consistently inside each cell at 2 μm below the contact point. Furthermore, cell membrane deformation recovered shortly after micropipette retrieval out of the cell by the system (0.47 ± 0.04 s, $n = 20$ cells).

Measurement of gap junction function in the diseased heart is an important area of research because of the role of gap junctions in passive electrical coupling between neighboring cardiomyocytes and propagation of action potential across the myocardium (*39*). Cardiac gap junctions are composed of hemichannels, or connexons, formed by the oligomerization of six connexin molecules (primarily Cx43) (*40*). The permeability of Cx43 gap junctions has been shown to be influenced by various interconnected factors, including external mechanical stimuli, intracellular ion concentrations, and posttranslational protein modifications (*41*–*43*). We found that increasing mechanical stimulation of the cell membrane, by increasing the depth of microinjection, reduced gap junction permeability. We speculate that microinjection activates stretch-induced calcium release pathways (*44*). Previous studies have shown that Ca^{2+} can bind gating sites on connexin hemichannels, leading to pore closure, which is thought to occur as a self-limiting mechanism for cell-cell Ca^{2+} diffusion (*45*). The binding of Ca^{2+} to Cx43 gating sites leads to

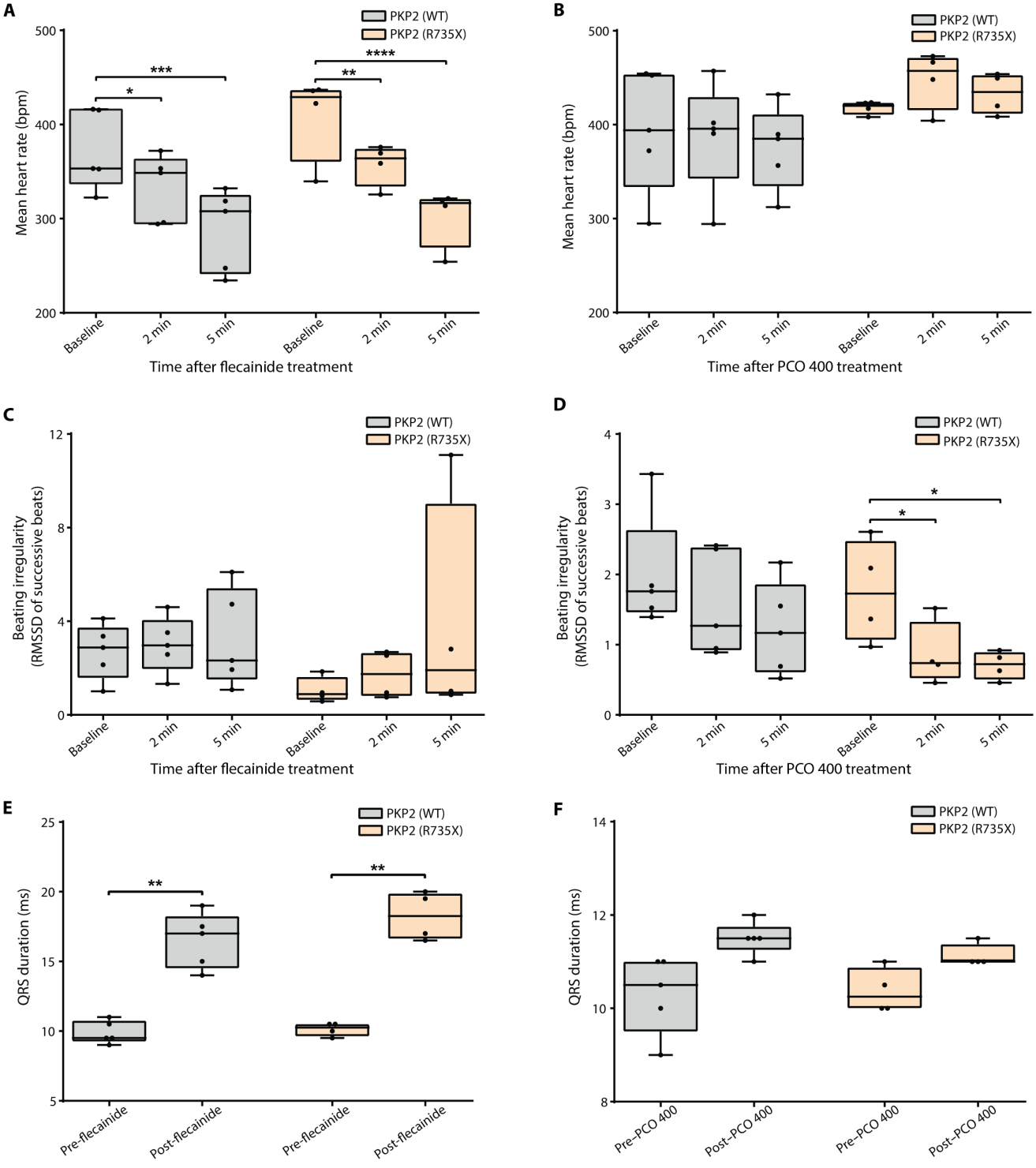

Fig. 5. PCO 400 reduces beating irregularity in mice expressing PKP2 (R735X). (**A** and **B**) Mean heart rate (in beats per minute), (**C** and **D**) heart rate variation (RMSSD), and (**E** and **F**) QRS duration (in milliseconds) for control AAV-PKP2–($n = 5$ mice) and mutant AAV-R735X–transduced ($n = 4$ mice) anesthetized mice at specific time points after a single dose of flecainide (20 mg/kg) or PCO 400 (1 mg/kg). [(A), (C), and (E)] Flecainide treatment reduced mean heart rate and increased QRS duration but did not improve heart rate variation in mice expressing either WT-PKP2 or PKP2-R735X. [(B), (D), and (F)] PCO 400 did not significantly alter mean heart rate or QRS duration but reduced beating irregularity (RMSSD of successive beats) in R735X mice. The box plot indicates the complete range (whiskers), interquartile range (box), and median (line) of the measurement. Statistics were calculated via a matched two-tailed Student's *t* test or a matched one-way ANOVA with a Dunnett's multiple comparisons post hoc test (*$P < 0.05$, **$P < 0.01$, ***$P < 0.001$, and ****$P < 0.0001$).

the closure of gap junctions and decreased dye diffusion between cells. However, we found this to be a transient effect because cardiomyocytes recovered gap junction permeability to baseline levels within 6 min of microinjection pipette withdrawal, likely because of the spontaneous release of Ca^{2+} from gating sites after the removal of mechanical stimulus.

In preclinical models of ACM, a loss in PKP2 has been correlated with a reduction in Cx43 surface expression at the intercalated disc, as well as a decrease in gap junction intercellular communication (*8*). Consistent with previous studies, we observed a reduction in gap junction permeability, as measured by dye transfer, in spontaneously beating iPSC-CM monolayers after *PKP2* knockdown. We have also recently demonstrated that *PKP2* knockdown cells have reduced conduction velocity and a higher variance in beating trajectories relative to wild-type cells, indicative of cell-to-cell conduction defects and irregularity in cell beating (*24*). These findings highlight an arrhythmic phenotype that arises from perturbed gap junction function and electrical coupling between cardiomyocytes. In addition, knockout of *PKP2* in mice has been shown to disrupt mechanical coupling between cells and alter the expression of calcium handling genes, resulting in contractility defects (*46*). We similarly observed decreased contractility in iPSC-CMs with *PKP2* knockdown, which may be attributable to changes in mechanical coupling between cells and dysregulation of calcium handling due to the loss of PKP2. The findings of our work reflect a number of pathologic changes that occur in the hearts of patients with ACM (*47*). Notably, certain disease-causing mutations, including *PKP2* mutations, have been correlated with defects in conduction pathways of the myocardium, resulting in delayed signal propagation and discontinuous conduction within subregions of the affected ventricle (*47*). These conduction abnormalities contribute to contractile dysfunction and arrhythmogenesis in patients with ACM and can potentially be targeted to reduce the incidence of sudden cardiac death.

Despite the known involvement of gap junction dysfunction in ACM pathogenesis, relatively few studies have explored the modulation of gap junction permeability as a therapeutic avenue for the disease. Although gap junctions have traditionally been considered an undesirable drug target because of variable isoform expression of connexins and the risk of nonspecific molecular effects, recent studies from multiple cancer research groups have demonstrated that small-molecule modulation of gap junction pores can be well tolerated in preclinical disease models and an effective treatment approach overall (*48*, *49*). In the field of cardiac research, extensive work has been done to characterize the effects of rotigaptide, a peptide modifier of gap junctions (*50*). Rotigaptide treatment has been shown to decrease the incidence of spontaneous arrhythmias in animal models of cardiac injury without causing drug-related toxicity (*51*, *52*). On the basis of the precedents set by these studies, we performed a targeted screen on beating iPSC-CM monolayers after *PKP2* knockdown using our automated robotic microinjection assay. Because gap junction permeability is sensitive to intracellular ion concentrations (*31*), the library we chose to screen consisted of drugs known to modulate ion channel activity (including drugs already licensed for clinical use).

From the screen, we identified five hits, some of which were not previously known to affect gap junction permeability. Flecainide, an antagonist of the Nav1.5 sodium channel (*29*, *53*), was an intriguing result because the drug has recently gained traction as an antiarrhythmic treatment for patients with ACM. Both preclinical and clinical studies have demonstrated that flecainide can reduce the burden of ventricular arrhythmias in affected individuals (*53*). The results of these studies have prompted a randomized clinical trial (NCT03685149) to determine the safety and efficacy of flecainide in patients with ACM. Consistent with prior studies, we noted a flecainide-induced decrease in mean heart rate and an increase in QRS interval duration due to sodium channel blockade by the drug. In contrast with a previous report, which noted antiarrhythmic effects of flecainide in mice with cardiac-specific knockout of *PKP2* (*46*), flecainide did not mitigate arrhythmias in our study. However, this discrepancy in results is likely due to differences in study design—the previous report induced arrhythmias by isoproterenol in mice with *PKP2* knockout, and animals were treated with a higher dose of flecainide (40 mg/kg), whereas our study monitored unstressed mice expressing mutant PKP2 (R735X) to identify spontaneous changes in beating irregularity. The antiarrhythmic effects of certain drugs, such as flecainide, may only be observable under conditions of isoproterenol or exercise-induced stress. Other identified hits from the robotic screen were found to affect potassium channels, including PCO 400, which is an agonist of adenosine triphosphate (ATP)–sensitive K^+ channels (K_{ATP}). Previous studies have found that K_{ATP} agonists can restore gap junction coupling of cardiomyocytes and mitigate arrhythmias in rodent models of cardiac injury and disease (*54*). Consistent with these findings, we observed PCO 400–mediated enhancement of gap junction permeability in iPSC-CMs with *PKP2* knockdown and reduced beating irregularity in mice expressing mutant PKP2 (R735X). In future experiments, it will be important to validate the effects of K_{ATP} agonists, such as PCO 400, on connexin-43 phosphorylation, protein levels, and cellular localization in cardiomyocytes. In addition, it will be necessary to delineate the effects of these drugs on cellular ion flux and gap junction coupling when evaluating their antiarrhythmic mechanism.

In summary, we developed a robotic microinjection assay to quantify beating iPSC-CMs' gap junction permeability. The robotic system was applied toward a clinically relevant model of ACM generated by shRNA knockdown of *PKP2* expression in spontaneously beating monolayers of iPSC-CMs and identified five compounds that enhanced gap junction permeability. We identified PCO 400 as a lead candidate from our screen and found that this drug reduced beating irregularity in a mouse model of ACM expressing mutant PKP2 (R735X). Future investigation into PCO 400 and other screening hits may provide important insight into pathways related to ACM disease progression and arrhythmogenesis. This will be especially important given the current lack of disease-modifying therapies and limited treatment options for ACM. Although gap junction dysfunction has long been recognized as a contributing factor in many human diseases, the notion of modulating gap junction function is an emerging and promising treatment paradigm. Our robotic microinjection assay provides a suitable platform for future screening of drugs across different cardiomyocytes and disease models to identify innovative gap junction–focused therapies.

MATERIALS AND METHODS

Robotic system setup

The setup of the system is shown in Fig. 1A and fig. S1. A DHM module was integrated into a Nikon Ti-S inverted microscope with a ×20 magnification, 0.45–numerical aperture objective (Nikon

Canada Inc., Canada) to simultaneously acquire bright-field images and holographic images. Both images were subsequently processed by a custom C++ MFC program, with the incorporation of the Lyncée Tec Software Development Kit (version 9.1.19516, Lyncee Tec SA, Switzerland) running on a personal computer (CPU: Intel Xeon W-2123, RAM: 16-gigabyte DDR4, graphic card: Nvidia GTX 1650, OS: Windows 10 Professional 64). Bright-field images were captured at a rate of 30 Hz using a complementary metal-oxide semiconductor camera (Ximea MC023MG-GY). Digital holograms were captured with a DHM camera module (Lyncee Tec SA DHM-C-P, Switzerland).

The motorized XY translational stage (ProScan, Prior Scientific, Inc.) in the system has a travel range of 75 mm along both axes with a resolution of 0.1 μm, a maximum speed of 5 mm/s, and a repeatability of 1.0 μm. The injection micropipette was mounted on a motorized four-axis micromanipulator (MX7600, Siskiyou, Inc.) with built-in encoders. The travel range is 30 mm, and the positioning resolution is 0.1 μm along each of the x, y, z, and tilt axes. A transparent heating plate (mTCII, Cell MicroControls) was mounted on the XY stage to control environmental temperature during dye injection.

A customized Z-shaped micropipette was created for the injection of adherent cells at a tilting angle of 45° in microwells. A standard capillary glass tube with an inner diameter of 0.78 mm and an outer diameter of 1 mm (Sutter Instrument Co.) was pulled using the Sutter Puller (Model P-97 Flaming/Brown micropipette puller, Sutter Instrument Co.) under the operational parameters shown in table S2. This generated a tip with an outer diameter of 500 nm and an inner diameter of 300 nm. A bending angle α (see Fig. 1B) was made at the point with a distance $L1$ (1 mm) to the tip using a microforge (Micro-forge 0810, TPI Technical Products International, Inc.). The length of $L1$ (1 mm) was experimentally determined, such that it was not too long to reduce micropipette tip stiffness or too short to allow for precise control over the bending angle. Using a customized alcohol lamp, which provides a small enough flame to heat and soften local areas of the micropipette body, a reverse angle α was made at the point with a distance $L2$ (1 cm) to the upper tip, such that the tip remained parallel with the main body of the glass tube. After mounting the micropipette on the robotic manipulator, α was set at 45° to make the two bending points of the micropipette parallel to the vertical wall of the 96-well plate (Fig. 1B and fig. S1). This increased the working space of the micropipette in the well.

DHM-based cell height calculation

For digital holographic imaging, an illumination laser source with a wavelength of λ = 666 nm (LynceeTec SA, Lausanne, Switzerland) was used. The laser source was divided by a beam splitter into an object beam to illuminate the sample and a reference beam that propagated through an optical fiber without interacting with the sample. The object and reference beams cohered at the imaging plane with a slight tilt angle, creating a hologram in a typical off-axis DHM configuration.

Once a digital hologram was acquired, a fast Fourier transform was applied to convert the hologram from the spatial domain to the frequency domain. Subsequently, a filter was used to isolate the component corresponding to the real image only. The quantitative phase-contrast image was then reconstructed using the filtered hologram via a reconstruction algorithm (*55*). The reconstructed wavefront in the Fresnel approximation is expressed as

$$\Psi(m,n) = A\Phi(m,n)\exp\left[\frac{i\pi}{\lambda d}\left(m^2\Delta\xi^2 + n^2\Delta\eta^2\right)\right]\times \\ \mathrm{FFT}\left\{\mathbf{R}_D(k,l)I_{\mathrm{FH}}(k,l)\times\exp\left[\frac{i\pi}{\lambda d}\left(k^2\Delta x^2 + l^2\Delta y^2\right)\right]\right\}_{m,n} \quad (1)$$

where A is a complex constant; $\Phi(m, n)$ is the digital phase mask for digital correction of the phase aberrations (*55*); λ is the wavelength; d is the reconstruction distance; $\Delta\xi$ and $\Delta\eta$ are the sampling intervals in the observation plane; k, l, m, and n are integers ($-N/2 \le m$, n, k, $l \le N/2$, and $N \times N$ is the number of recorded pixels by the camera: 800 pixels by 800 pixels); FFT is the fast Fourier transform; $\mathbf{R}_D$ is the digital reference wave; I_{FH} is the filtered hologram; and Δx and Δy are the sampling intervals in the camera plane. Eventually, the phase image is obtained by

$$\phi(m,n) = \arctan\left\{\frac{\mathrm{Im}[\Psi(m,n)]}{\mathrm{Re}[\Psi(m,n)]}\right\} \quad (2)$$

Also, the phase unwrapping algorithm (*56*) was implemented to avoid a potential phase jump. The phase image contains object beam waveform information, which is related to the optical path length OPL by

$$\mathrm{OPL}_i = \frac{\lambda\phi_i}{2\pi} \quad (3)$$

where OPL_i and ϕ_i are the optical path length and phase value at the position of pixel i, respectively. The optical path length can also be expressed in terms of the specimen's physical properties as

$$\mathrm{OPL}_i = \int_0^{h_i} n_{c,i}(z)dz + n_m\left(D - h_i\right) = \left(\overline{n}_{c,i} - n_m\right)h_i + n_m D \quad (4)$$

where z is the depth coordinate, h_i is the cardiomyocyte height corresponding to the position of pixel i, $n_{c,i}(z)$ is the intracellular refractive index at the position of pixel i and height z to the substrate, $n_m = 1.345$ is the refractive index of the perfusion medium, D is the height of the medium, and $\overline{n}_{c,i} = \frac{1}{h_i}\int_0^{h_i} n_c(z)dz$ is the average refractive index along the cardiomyocyte height. By matching the confocal images and quantitative phase images, the actual cardiomyocyte height and the corresponding difference in optical path length can be obtained, and thus $\overline{n}_{c,i}$ can be calculated at different cellular positions. Considering that the intracellular refractive index has a relatively small variance among different locations of a cardiomyocyte, a mean intracellular refractive index of $\overline{n}_c = 1.380 \pm 0.005$ was used in our study. Thus, the relative cell height at pixel i of frame p to pixel j at frame q is

$$h_{ip,jq} = \frac{\mathrm{OPL}_{i,p} - \mathrm{OPL}_{j,q}}{\overline{n}_c - n_m} \quad (5)$$

With GPU acceleration, the entire process of acquiring a quantitative phase image acquisition was completed within 60 ms to guarantee >10-Hz cell height feedback in the control loop. The theoretical resolution of height measurement in the z axis is $R_{(Z)} \approx$ 106 nm, which corresponds to a spatial variance of phase of 2°.

Robotic microinjection of iPSC-CMs to assess gap junction permeability

A protocol for robotic microinjection of iPSC-CMs was developed to efficiently measure gap junction permeability and facilitate small-molecule screening to identify gap junction modulators. To operate the system, all actions were performed remotely through computer mouse clicking. Before microinjection, contact detection of the *z* position of the substrate surface was conducted in an empty well of the 96-well plate. The micropipette was then moved to the targeted cell culture well and moved down to a *z* position of 10 μm above the substrate surface (experimentally determined as a safe distance to prevent touching the cell surface when moving horizontally). iPSC-CM monolayer height values relative to the substrate surface were calculated from the DHM images. During microinjection, the operator selected multiple targeted cells within the field of view of the DHM image. The software performed nucleus segmentation using a high-pass filter after a Canny edge detector and fitting the minimum ellipse enclosing the detected edges. The microinjection location for each cell was set at a lateral distance of 3 μm from the nucleus boundary to ensure dye diffusion in the cytoplasm and avoid nucleus damage during microinjection. Vertical displacement of beating iPSC-CMs was monitored by tracking the cell height differences from DHM images (Fig. 1H), and dye microinjection was conducted in the resting phase when vertical displacement was below the threshold value of 0.05 μm. Once the targeted iPSC-CMs entered the resting phase, the micropipette was moved down at 300 μm/s until it contacted the cell's top surface and then injected the cell to a predefined depth of 2 μm (see movie S3). The volume of dye solution injected (25 fl) was controlled by administering a gas pulse with a specific pressure (2500 hPa) and duration (0.2 s) to the micropipette. The average speed of microinjection was 20 cells/min. The time cost of each step is summarized in table S3. The average error of the injected dye solution was determined to be less than 1% of the total volume of dye injected per cell. Cell viability was measured using calcein AM (2 μM). Cardiomyocytes that were positive for propidium iodide (in the red channel) and calcein (in the green channel) were considered live, whereas microinjected cells that were only positive for PI were considered dead.

Quantification of gap junction permeability by dye transfer

Cardiomyocytes were injected with propidium iodide, a membrane-impermeable fluorescent dye that solely diffuses between cells through gap junctions. After successful microinjection, injected iPSC-CMs were moved to the center of the microscope's field of view on the basis of recorded cell positions. Fluorescent images were collected 6 min after injection to allow sufficient time for cells to recover from microinjection and for dye transfer to occur. Dye transfer was quantified from the number of cells with a nucleus positive for fluorescent signal (excluding the microinjected cell). Because the amount of dye deposited by microinjection and the sensitivity of microscopy imaging can influence dye transfer measurement, we accurately controlled the dye concentration (0.5 mg/ml) and injection volume (25 fl) for each microinjection and used consistent fluorescence imaging conditions, including laser intensity and exposure time. Relative dye transfer was determined as a ratio of dye transfer in drug-treated cells compared to dye transfer in control-treated cells.

Cells, reagents, and materials

Human iPSC-CMs (iCell Cardiomyocytes^2) were obtained from Fujifilm Cellular Dynamics International in a cryopreserved state. Cells were thawed and maintained as per the manufacturer's protocol and distributed on 96-well plates coated with 0.1% w/v gelatin (G1890, MilliporeSigma). Cells were cultured at 37°C, 5% CO_2 until the cardiomyocytes formed a confluent, synchronously beating monolayer suitable for compound addition and experimentation. All of the following compounds were obtained and stored as concentrated stocks in DMSO: Cilostamide (sc-201180), CAPE (sc-200800), lycopene (sc-205738), liarozole (sc-204055), and 18-αGA (sc-223188) were acquired from Santa Cruz Biotechnology. Carvedilol (C3993) and nifedipine (N7634) were purchased from MilliporeSigma. Omecamtiv mecarbil (CK-1827452) was purchased from Selleck Chemicals. Rotigaptide (ZP-123) was acquired from China Peptides Co. Ltd. PQ1, PQ7, and PQ15 were provided by the laboratory of D. H. Hua. Calcein AM (C1430) was purchased from Thermo Fisher Scientific. The SCREEN-WELL Ion Channel ligand library (BML-2805) was purchased from Enzo Life Sciences. Each drug was diluted to the appropriate concentration for experimentation in iCell Maintenance Medium (Fujifilm Cellular Dynamics International), and the final ratio of DMSO in each well was lower than 0.1% v/v.

Lentiviral knockdown of PKP2 by shRNA

shRNA constructs targeting *PKP2* were obtained from the Dharmacon GIPZ lentiviral shRNA library (GE Healthcare) and packaged into lentivirus by SPARC BioCentre (Hospital for Sick Children, Canada). Monolayers of iPSC-CMs were transduced with the lentivirus 5 days after seeding, and transduction efficiency was monitored by fluorescence of a green fluorescent protein reporter. Knockdown at the protein level was confirmed 14 days after transduction by Western blot using a mouse monoclonal PKP2 antibody (8H6, Abcam) diluted 1:100 in 0.1% PBST (phosphate-buffered saline with 0.1% Tween-20). Protein levels were quantified by densitometry on Western blot images using the open-source software ImageJ (v1.52b).

Monitoring of cardiomyocyte beating rate and amplitude

The xCelligence RTCA CardioECR is a multiple electrode array–based platform designed for label-free, continuous real-time monitoring of cardiomyocyte beat rate, rhythm, and amplitude by impedance-based measurements. iPSC-CMs were seeded to an E-Plate Cardio 96 (ACEA Biosciences, Inc.) coated with fibronectin (10.0 μg/ml; 356008, Corning). Lentiviral transduction was performed 5 days after seeding, at which point the cells had fully attached to the plate and formed synchronously beating monolayers. Cardiomyocytes were either transduced with *PKP2* shRNA or a nonsilencing control. Data on contractile dynamics were collected in real time over the next 3 weeks to determine the effects of *PKP2* knockdown on iPSC-CMs. Cells were paced at a frequency of 1.5 Hz to eliminate potential confounding effects of beat rate on beat amplitude.

Immunofluorescence/live staining and microscopy of iPSC-CMs

iPSC-CMs were seeded in flat, microclear-bottom 96-well plates (655096, Greiner Bio-One) coated with 0.1% w/v gelatin (G1890, Sigma-Aldrich). Lentiviral transduction was performed 5 days after

seeding. At 14 days after transduction, cells were fixed in 4% paraformaldehyde for 20 min and permeabilized with 0.3% Triton X-100 for 10 min at room temperature. Connexin-43 and α-actinin were probed using a rabbit anti–connexin-43 antibody (1:250 dilution; 3512S, Cell Signaling Technology) and a mouse anti–α-actinin antibody (1:500 dilution; ab9465, Abcam) with an overnight incubation at 4°C on a rocking platform. The following day, cells were washed with 0.1% PBST and incubated with anti-rabbit Fab fragment–Alexa Fluor 594 conjugate (8889S, Cell Signaling Technology), anti-mouse Fab fragment–Alexa Fluor 647 conjugate (4410S, Cell Signaling Technology), and Hoechst 33342 (1 μg/ml; H3570, Thermo Fisher Scientific) for 1 hour at room temperature. Cell height was measured via live staining of iPS-CMs by adding Hoechst 33342 (1 μg/ml; H3570, Thermo Fisher Scientific), CellMask Green (5 μg/ml; C37608, Invitrogen) and calcein (2 μM; C3099, Invitrogen) for 10 min at 37°C. The micropipette tip was fluorescently labeled with Alexa Fluor 647–BSA (A34785, Invitrogen). Fluorescent images were captured using a spinning disk confocal system (CSU-W1, Nikon) at ×40 magnification.

Screening of compounds by robotic microinjection to identify enhancers of gap junction permeability in iPSC-CMs with *PKP2* knockdown

Lentiviral transduction with *PKP2* shRNA and nonsilencing controls was performed 5 days after seeding. At 14 days after transduction, 70 compounds from the SCREEN-WELL ion channel ligand library and six additional known modifiers of cardiac activity or gap junction permeability (omecamtiv mecarbil, carvedilol, nifedipine, PQ1, PQ7, and PQ15) were added to the cells at a final concentration of 10.0 μM (final DMSO concentration of 0.1% v/v). Cells were drug-treated for 24 hours before the measurement of dye transfer by our robotic microinjection assay. Subsequent generation of dose-response curves for each screening hit was performed under the same conditions at multiple drug concentrations.

Adeno-associated virus vector production and purification

All adeno-associated virus (AAV) vectors were produced by the triple transfection method using human embryonic kidney (HEK) 293T cells (American Type Culture Collection), as described previously (*25*). AAV plasmids were cloned and propagated in *Escherichia coli* strain Stbl3 (Life Technologies). Shuttle plasmids *pAAV-PKP2* and *pAAV-R735X* were packaged into AAV-9 capsids with the use of the helper plasmids *pAdDF6* (providing the three adenoviral helper genes) and *pAAV2/9* (providing rep and cap viral genes), obtained from PennVector. The AAV shuttle and helper plasmids were transfected into HEK293T cells via calcium phosphate coprecipitation. A total of 840 μg of equimolar-mixed plasmid DNA was used per HYPERFlask (Corning) seeded with 1.2×10^8 cells the day before. Seventy-two hours after transfection, the cells were collected by centrifugation, and the cell pellet was resuspended in TMS (50 mM tris-HCl, 150 mM NaCl, and 2 mM $MgCl_2$) on ice before digestion with DNase I and RNase A (0.1 mg/ml each; Roche) at 37°C for 60 min. A clarified supernatant containing the viral particles was obtained by iodixanol gradient centrifugation (*57*). Virus-containing gradient fractions were concentrated through Amicon UltraCel columns (MilliporeSigma) and stored at−80°C.

AAV injection of mice

Four- to six-week-old wild-type C57BL6/J mice were anesthetized with a 100.0-μl intraperitoneal injection containing ketamine (60.0 mg/kg), xylazine (20.0 mg/kg), and atropine (9.0 mg/kg). Once anesthetized, animals were placed on a heated pad at 37.0 ± 0.5°C to prevent hypothermia. A small incision (4 mm) was made to expose the right femoral vein. To increase vessel diameter and facilitate infusion, blood flow was interrupted with a cotton bud for a few seconds. Once the vein was dilated, an insulin syringe vessel was introduced into the vein, and 5×10^{10} virus particles were injected in a volume of 50.0 μl, taking care to prevent the introduction of air bubbles. Subcutaneous buprenorphine (0.1 mg/kg) was then administered for analgesia, and animals were maintained on the heated pad until recovery. Paracetamol was administered orally for 1 week after surgery.

ECG recording of mice

Mice were anesthetized using isoflurane inhalation (0.8 to 1.0% volume in oxygen), and the efficacy of the anesthesia was monitored by respiration rate. Four-lead surface ECGs were recorded, for a period of 5 min, from subcutaneous 23-gauge needle electrodes attached to each limb using the MP36R amplifier unit (BIOPAC Systems). During offline analysis, lead II was used for automated ECG analysis in PhysioData Toolbox (v0.5.0) (Leiden University, Netherlands). QRS duration [before and after intraperitoneal administration of flecainide (20 mg/kg) or PCO 400 (1 mg/kg)] was measured as the time interval between the earliest moment of deviation from baseline and the moment when the S-wave returned to the isoelectric line.

Mouse study approval

All experimental and other scientific procedures using animals conformed to EU Directive 2010/63EU and Recommendation 2007/526/EC, enforced in Spanish law under Real Decreto 53/2013. All animal experiments were conducted in accordance with the CNIC Institutional Ethics Committee's recommendations and were approved by the Animal Experimentation Committee of the Animal Protection Area of the Comunidad Autónoma de Madrid (PROEX 019/17).

Statistics

Statistical analyses were performed in GraphPad Prism (v6.0) (GraphPad software) by a two-tailed Student's *t* test or a one-way analysis of variance (ANOVA) with a Dunnett's multiple comparisons post hoc test, unless otherwise specified. All values within the manuscript are presented as means ± SEM. The box plot indicates the complete range (whiskers), interquartile range (box), and median (line) of the measurement. Significant differences between groups of data are represented as $^*P < 0.05$, $^{**}P < 0.01$, $^{***}P < 0.001$, and $^{****}P < 0.0001$.

Supplementary Materials

The PDF file includes:

Figs. S1 to S11
Tables S1 to S3

Other Supplementary Material for this manuscript includes the following:

Movies S1 to S4
MDAR Reproducibility Checklist

REFERENCES AND NOTES

1. D. Corrado, C. Basso, D. P. Judge, Arrhythmogenic cardiomyopathy. *Circ. Res.* **121**, 784–802 (2017).
2. C. Basso, F. Calabrese, D. Corrado, G. Thiene, Postmortem diagnosis in sudden cardiac death victims: Macroscopic, microscopic and molecular findings. *Cardiovasc. Res.* **50**, 290–300 (2001).
3. K. A. Jacob, M. Noorman, M. G. P. J. Cox, J. A. Groeneweg, R. N. W. Hauer, M. A. G. van der Heyden, Geographical distribution of plakophilin-2 mutation prevalence in patients with arrhythmogenic cardiomyopathy. *Neth. Heart J.* **20**, 234–239 (2012).
4. P. Elliott, C. O'Mahony, P. Syrris, A. Evans, C. R. Sorensen, M. N. Sheppard, G. Carr-White, A. Pantazis, W. J. McKenna, Prevalence of desmosomal protein gene mutations in patients with dilated cardiomyopathy. *Circ. Cardiovasc. Genet.* **3**, 314–322 (2010).
5. X. Chen, S. Bonné, M. Hatzfeld, F. Van Roy, K. J. Green, Protein binding and functional characterization of plakophilin 2: Evidence for its diverse roles in desmosomes and β-catenin signaling. *J. Biol. Chem.* **277**, 10512–10522 (2002).
6. E. Agullo-Pascual, D. A. Reid, S. Keegan, M. Sidhu, D. Fenyö, E. Rothenberg, M. Delmar, Super-resolution fluorescencemicroscopy of the cardiac connexome reveals plakophilin-2 inside the connexin43 plaque. *Cardiovasc. Res.* **100**, 231–240 (2013).
7. S. Rohr, Role of gap junctions in the propagation of the cardiac action potential. *Cardiovasc. Res.* **62**, 309–322 (2004).
8. E. M. Oxford, H. Musa, K. Maass, W. Coombs, S. M. Taffet, M. Delmar, Connexin43 remodeling caused by inhibition of plakophilin-2 expression in cardiac cells. *Circ. Res.* **101**, 703–711 (2007).
9. J. Sugita, K. Fujiu, Y. Nakayama, T. Matsubara, J. Matsuda, T. Oshima, Y. Liu, Y. Maru, E. Hasumi, T. Kojima, H. Seno, K. Asano, A. Ishijima, N. Tomii, M. Yamazaki, F. Kudo, I. Sakuma, R. Nagai, I. Manabe, I. Komuro, Cardiac macrophages prevent sudden death during heart stress. *Nat. Commun.* **12**, 1910 (2021).
10. A. Dydowiczová, O. Brózman, P. Babica, I. Sovadinová, Improved multiparametric scrape loading-dye transfer assay for a simultaneous high-throughput analysis of gap junctional intercellular communication, cell density and viability. *Sci. Rep.* **10**, 730 (2020).
11. Y. Zhang, Microinjection technique and protocol to single cells (Protocol Exchange, 2007); https://doi.org/10.1038/nprot.2007.487.
12. W. Wang, Y. Sun, M. Zhang, R. Anderson, L. Langille, W. Chan, A system for high-speed microinjection of adherent cells. *Rev. Sci. Instrum.* **79**, 104302 (2008).
13. J. Liu, V. Siragam, Z. Gong, J. Chen, M. D. Fridman, C. Leung, Z. Lu, C. Ru, S. Xie, J. Luo, R. M. Hamilton, Y. Sun, Robotic adherent cell injection for characterizing cell-cell communication. *IEEE Trans. Biomed. Eng.* **62**, 119–125 (2015).
14. W. H. Wang, X. Y. Liu, Y. Sun, Contact detection in microrobotic manipulation. *Int. J. Rob. Res.* **26**, 821–828 (2007).
15. J. Liu, Z. Zhang, X. Wang, H. Liu, Q. Zhao, C. Zhou, M. Tan, H. Pu, S. Xie, Y. Sun, Automated robotic measurement of 3-D cell morphologies. *IEEE Robot. Autom. Lett.* **2**, 499–505 (2017).
16. A. Mo, H. Lin, Z. Wen, W. Lu, X. Long, Y. Zhou, Efficacy and safety of on-pump beating heart surgery. *Ann. Thorac. Surg.* **86**, 1914–1918 (2008).
17. K. Jaferzadeh, B. Rappaz, F. Kuttler, B. K. Kim, I. Moon, P. Marquet, G. Turcatti, Marker-free automatic quantification of drug-treated cardiomyocytes with digital holographic imaging. *ACS Photonics* **7**, 105–113 (2020).
18. J. Hajduk, K. Szajna, B. Lisowski, Z. Rajfur, The influence of microinjection parameters on cell survival and procedure efficiency. *MethodsX* **10**, 102107 (2023).
19. P. Ridone, M. Vassalli, B. Martinac, Piezo1 mechanosensitive channels: What are they and why are they important. *Biophys. Rev.* **11**, 795–805 (2019).
20. E. J. Behringer, M. J. Socha, L. Polo-Parada, S. S. Segal, Electrical conduction along endothelial cell tubes from mouse feed arteries: Confounding actions of glycyrrhetinic acid derivatives. *Br. J. Pharmacol.* **166**, 774–787 (2012).
21. F. F. Bukauskas, R. Weingart, Temperature dependence of gap junction properties in neonatal rat heart cells. *Pflugers Arch.* **423**, 133–139 (1993).
22. I. El-Battrawy, S. Lang, Z. Zhao, I. Akin, G. Yücel, S. Meister, B. Patocskai, M. Behnes, B. Rudic, E. Tülümen, V. Liebe, M. Tiburcy, J. Dworacek, W.-H. Zimmermann, J. Utikal, T. Wieland, M. Borggrefe, X.-B. Zhou, Hyperthermia influences the effects of sodium channel blocking drugs in human-induced pluripotent stem cell-derived cardiomyocytes. *PLOS ONE* **11**, e0166143 (2016).
23. K. Obata, H. Morita, M. Takaki, Mechanism underlying the negative inotropic effect in rat left ventricle in hyperthermia: The role of TRPV1. *J. Physiol. Sci.* **70**, 4 (2020).
24. W. Dou, Q. Zhao, M. Malhi, X. Liu, Z. Zhang, L. Wang, S. Masse, K. Nanthakumar, R. Hamilton, J. T. Maynes, Y. Sun, Label-free conduction velocity mapping and gap junction assessment of functional iPSC-Cardiomyocyte monolayers. *Biosens. Bioelectron.* **167**, 112468 (2020).
25. F. M. Cruz, D. Sanz-Rosa, M. Roche-Molina, J. García-Prieto, J. M. García-Ruiz, G. Pizarro, L. J. Jiménez-Borreguero, M. Torres, A. Bernad, J. Ruíz-Cabello, V. Fuster, B. Ibáñez, J. A. Bernal, Exercise triggers ARVC phenotype in mice expressing a disease-causing mutated version of human plakophilin-2. *J. Am. Coll. Cardiol.* **65**, 1438–1450 (2015).
26. A. Asimaki, J. E. Saffitz, Remodeling of cell-cell junctions in arrhythmogenic cardiomyopathy. *Cell Commun. Adhes.* **21**, 13–23 (2014).
27. J. Bernzweig, B. Heiniger, K. Prasain, J. Lu, D. H. Hua, T. A. Nguyen, Anti-breast cancer agents, quinolines, targeting gap junction. *Med. Chem.* **7**, 448–453 (2011).
28. M. Karakaya, Y. Sert, M. Kürekçi, B. Eskiyurt, Ç. Çirak, Theoretical and experimental investigations on vibrational and structural properties of tolazamide. *J. Mol. Struct.* **1095**, 87–95 (2015).
29. E. Ramos, M. E. O'Leary, State-dependent trapping of flecainide in the cardiac sodium channel. *J. Physiol.* **560**, 37–49 (2004).
30. H. Ikenaga, J. P. Bast, R. W. Fallet, P. K. Carmines, Exaggerated impact of ATP-sensitive K^+ channels on afferent arteriolar diameter in diabetes mellitus. *J. Am. Soc. Nephrol.* **11**, 1199–1207 (2000).
31. F. F. Bukauskas, V. K. Verselis, Gap junction channel gating. *Biochim. Biophys. Acta* **1662**, 42–60 (2004).
32. M. A. M. Van Steensel, Gap junction diseases of the skin. *Am. J. Med. Genet.* **131C**, 12–19 (2004).
33. H. J. Donahue, R. W. Qu, D. C. Genetos, Joint diseases: From connexins to gap junctions. *Nat. Rev. Rheumatol.* **14**, 42–51 (2018).
34. P. Wong, V. Laxton, S. Srivastava, Y. W. Fiona Chan, G. Tse, The role of gap junctions in inflammatory and neoplastic disorders (review). *Int. J. Mol. Med.* **39**, 498–506 (2017).
35. H. Takeuchi, A. Suzumura, Gap junctions and hemichannels composed of connexins: Potential therapeutic targets for neurodegenerative diseases. *Front. Cell. Neurosci.* **8**, 189 (2014).
36. B. Tamadazte, N. L. F. Piat, S. Dembélé, Robotic micromanipulation and microassembly using monoview and multiscale visual servoing. *IEEE ASME Trans. Mechatron.* **16**, 277–287 (2011).
37. Z. Zhang, X. Wang, J. Liu, C. Dai, Y. Sun, Robotic micromanipulation: Fundamentals and applications. *Annu. Rev. Control Robot. Auton. Syst.* **2**, 181–203 (2019).
38. A. Shakoor, M. Xie, T. Luo, J. Hou, Y. Shen, J. K. Mills, D. Sun, Achieving automated organelle biopsy on small single cells using a cell surgery robotic system. *IEEE Trans. Biomed. Eng.* **66**, 2210–2222 (2019).
39. N. L. Tulloch, V. Muskheli, M. V. Razumova, F. S. Korte, M. Regnier, K. D. Hauch, L. Pabon, H. Reinecke, C. E. Murry, Growth of engineered human myocardium with mechanical loading and vascular coculture. *Circ. Res.* **109**, 47–59 (2011).
40. T. A. B. van Veen, H. V. M. van Rijen, T. Opthof, Cardiac gap junction channels: Modulation of expression and channel properties. *Cardiovasc. Res.* **51**, 217–229 (2001).
41. J. Zou, M. Salarian, Y. Chen, R. Veenstra, C. F. Louis, J. J. Yang, Gap junction regulation by calmodulin. *FEBS Lett.* **588**, 1430–1438 (2014).
42. A. Salameh, A. Wustmann, S. Karl, K. Blanke, D. Apel, D. Rojas-Gomez, H. Franke, F. W. Mohr, J. Janousek, S. Dhein, Cyclic mechanical stretch induces cardiomyocyte orientation and polarization of the gap junction protein connexin43. *Circ. Res.* **106**, 1592–1602 (2010).
43. A. C. Cone, G. Cavin, C. Ambrosi, H. Hakozaki, A. X. Wu-Zhang, M. T. Kunkel, A. C. Newton, G. E. Sosinsky, Protein kinase Cδ-mediated phosphorylation of connexin43 gap junction channels causes movement within gap junctions followed by vesicle internalization and protein degradation. *J. Biol. Chem.* **289**, 8781–8798 (2014).
44. K. Takahashi, S. Hayashi, M. Miyajima, M. Omori, J. Wang, K. Kaihara, M. Morimatsu, C. Wang, J. Chen, G. Iribe, K. Naruse, M. Sokabe, L-type calcium channel modulates mechanosensitivity of the cardiomyocyte cell line H9c2. *Cell Calcium* **79**, 68–74 (2019).
45. W. Lopez, J. Ramachandran, A. Alsamarah, Y. Luo, A. L. Harris, J. E. Contreras, Mechanism of gating by calcium in connexin hemichannels. *Proc. Natl. Acad. Sci. U.S.A.* **113**, E7986–E7995 (2016).
46. M. Cerrone, J. Montnach, X. Lin, Y.-T. Zhao, M. Zhang, E. Agullo-Pascual, A. Leo-Macias, F. J. Alvarado, I. Dolgalev, T. V. Karathanos, K. Malkani, C. J. M. Van Opbergen, J. J. A. van Bavel, H.-Q. Yang, C. Vasquez, D. Tester, S. Fowler, F. Liang, E. Rothenberg, A. Heguy, G. E. Morley, W. A. Coetzee, N. A. Trayanova, M. J. Ackerman, T. A. B. van Veen, H. H. Valdivia, M. Delmar, Plakophilin-2 is required for transcription of genes that control calcium cycling and cardiac rhythm. *Nat. Commun.* **8**, 106 (2017).
47. C. M. Andrews, N. T. Srinivasan, S. Rosmini, H. Bulluck, M. Orini, S. Jenkins, A. Pantazis, W. J. McKenna, J. C. Moon, P. D. Lambiase, Y. Rudy, Electrical and structural substrate of arrhythmogenic right ventricular cardiomyopathy determined using noninvasive electrocardiographic imaging and late gadolinium magnetic resonance imaging. *Circ. Arrhythm. Electrophysiol.* **10**, e005105 (2017).
48. T. Aasen, E. Leithe, S. V. Graham, P. Kameritsch, M. D. Mayán, M. Mesnil, K. Pogoda, A. Tabernero, Connexins in cancer: Bridging the gap to the clinic. *Oncogene* **38**, 4429–4451 (2019).
49. J.-I. Wu, L.-H. Wang, Emerging roles of gap junction proteins connexins in cancer metastasis, chemoresistance and clinical application. *J. Biomed. Sci.* **26**, 8 (2019).
50. A. L. Kjølbye, K. Haugan, J. K. Hennan, J. S. Petersen, Pharmacological modulation of gap junction function with the novel compound rotigaptide: A promising new principle for prevention of arrhythmias. *Basic Clin. Pharmacol. Toxicol.* **101**, 215–230 (2007).

51. J. K. Hennan, R. E. Swillo, G. A. Morgan, J. C. Keith, R. G. Schaub, R. P. Smith, H. S. Feldman, K. Haugan, J. Kantrowitz, P. J. Wang, A. Abu-Qare, J. Butera, B. D. Larsen, D. L. Crandall, Rotigaptide (ZP123) prevents spontaneous ventricular arrhythmias and reduces infarct size during myocardial ischemia/reperfusion injury in open-chest dogs. *J. Pharmacol. Exp. Ther.* **317**, 236–243 (2006).
52. Y.-C. Hsieh, J.-C. Lin, C.-Y. Hung, C.-H. Li, S.-F. Lin, H.-I. Yeh, J.-L. Huang, C.-P. Lo, K. Haugan, B. D. Larsen, T.-J. Wu, Gap junction modifier rotigaptide decreases the susceptibility to ventricular arrhythmia by enhancing conduction velocity and suppressing discordant alternans during therapeutic hypothermia in isolated rabbit hearts. *Heart Rhythm* **13**, 251–261 (2016).
53. F. Bouvier, C. Maupain, N. C. Roche, L. Fiorina, D. Poindron, C. Moini, E. Gandjbakhch, Effectiveness and safety of flecainide in arrhythmogenic right ventricular cardiomyopathy. *Arch. Cardiovasc. Dis. Suppl.* **10**, 98–99 (2018).
54. T.-M. Lee, C.-C. Lin, H.-Y. Lien, C.-C. Chen, K_{ATP} channel agonists preserve connexin43 protein in infarcted rats by a protein kinase C-dependent pathway. *J. Cell. Mol. Med.* **16**, 776–788 (2012).
55. E. Cuche, P. Marquet, C. Depeursinge, Simultaneous amplitude-contrast and quantitative phase-contrast microscopy by numerical reconstruction of Fresnel off-axis holograms. *Appl. Opt.* **38**, 6994–7001 (1999).
56. M. A. Herráez, D. R. Burton, M. J. Lalor, M. A. Gdeisat, Fast two-dimensional phase-unwrapping algorithm based on sorting by reliability following a noncontinuous path. *Appl. Opt.* **41**, 7437–7444 (2002).
57. W. W. Hauswirth, A. S. Lewin, S. Zolotukhin, N. Muzyczka, Production and purification of recombinant adeno-associated virus. *Methods Enzymol.* **316**, 743–761 (2000).

Acknowledgments: We thank D. H. Hua for providing the substituted quinolines (PQ1, PQ7, and PQ15) and SPARC BioCentre at the Hospital for Sick Children for generating the lentivirus. Graphical representations were created with BioRender.com. **Funding:** The work is supported by the Canadian Institute for Health Research (CIHR) and the Natural Sciences and Engineering Research Council of Canada (NSERC). Y.S. acknowledges support from the Canada Research Chairs program and the Ontario Research Fund - Research Excellence program. J.T.M. acknowledges support from the SickKids Foundation for chair funds. J.A.B. acknowledges funding from the MCIU under grant BFU2016-75144-R. **Author contributions:** W.D., G.S., Q.Z., M.M., X.L., Y.S., and J.T.M. conceived the project. G.S., Q.Z., A.J., and W.D. developed the robotic microinjection system. W.D. and M.M. conducted cell culture and related experiments. A.G.-G. and J.A.B. performed the animal studies. Z.Z., S.F., J.L., and R.M.H. conducted all other experiments. Y.S., J.T.M., and J.A.B. provided funding. W.D., G.S., M.M., Q.Z., Y.S., and J.T.M. analyzed the data and wrote the manuscript with input from all the authors. **Competing interests:** The authors declare that they have no competing interests. **Data and materials availability:** The authors declare that all data supporting the findings of this study are presented in the paper or the Supplementary Materials and are available online at DOI:10.5061/dryad.b8gtht7mz.

Submitted 7 November 2023
Accepted 26 September 2024
Published 23 October 2024
10.1126/scirobotics.adm8233

Science Robotics

Robotic manipulation of cardiomyocytes to identify gap junction modifiers for arrhythmogenic cardiomyopathy

Wenkun Dou, Guanqiao Shan, Qili Zhao, Manpreet Malhi, Aojun Jiang, Zhuoran Zhang, Andrés González-Guerra, Shaojie Fu, Junhui Law, Robert M. Hamilton, Juan A. Bernal, Xinyu Liu, Yu Sun, and Jason T. Maynes

Sci. Robot. **9** (95), eadm8233. DOI: 10.1126/scirobotics.adm8233

Editor's summary

The cardiac disease arrhythmogenic cardiomyopathy is associated with deficiencies in cell-to-cell adhesion and can result in sudden fatal arrhythmias. Researchers have attempted to study the gap junctions in cardiomyocytes but have largely relied on manual experimental techniques. Dou *et al*. have developed a robotic cell manipulation system capable of microinjecting cardiomyocytes, with the ability to offset the spontaneous beating of the cells. They used the robotic system to study the permeability of healthy and diseased cells and subsequently carried out a drug screen to identify potential drug targets for treating the disease, which was validated in an in vivo study showing the ability to reduce beating irregularities in mice. —Amos Matsiko